

Measurements of the concentration field in nonlinear travelling-wave convection

By BERNHARD L. WINKLER† AND PAUL KOLODNER

AT & T Bell Laboratories, Murray Hill, NJ 07974-2070, USA

(Received 15 August 1991)

We present observations of travelling-wave convection in ethanol/water mixtures in a rectangular container using shadowgraphic flow visualization along the axes of the convective rolls. The entrainment of solute into the centre of the fluid layer from the boundary layers at the top and bottom of the cell is clearly observed in the shadowgraph images as sharp features at the roll boundaries. The shadowgraph images are integrated to yield a map of the two-dimensional refractive-index field. The contributions to this field from the convective temperature and the concentration fields have sufficiently different spatial character to be reliably separated using image-processing techniques. This has allowed us to produce a map of these two flow fields that is in good quantitative agreement with numerical integrations of the full Navier–Stokes equations in the Boussinesq approximation. We also present qualitative visualizations of transients caused by abruptly triggering and quenching travelling-wave convection. These experiments illustrate the formation of concentration boundary layers and reveal the existence of large-scale currents which are an inherent part of travelling-wave convection.

1. Introduction

In the past several years, the problem of convection in a thin, horizontal layer of a binary fluid mixture which is heated from below has been the focus of an enormous amount of scientific activity. The principal reason for this interest is the fact that both the linear state to which the conducting fluid is unstable at onset and the nonlinear state which is triggered by this instability take the form of *travelling waves* (Walden *et al.* 1985; Kolodner *et al.* 1986; Surko & Kolodner 1987). Because these experiments can be controlled with extreme precision, and because the equations which describe this system are well understood, binary-fluid convection is an excellent system in which to study the nonlinear dynamics of travelling waves. Indeed, a wealth of fascinating travelling-wave patterns has been studied in such experiments (for references to recent work, consult Moses & Steinberg 1989; Kolodner 1990; Barten, Lücke & Kamps 1991; Steinberg & Kaplan 1991).

Despite this enormous amount of attention it is only recently that theoretical understanding has evolved to the point of quantitatively explaining why nonlinear convective rolls in binary fluids propagate in the first place. In this system, the primary experimental parameter is, as usual, the Rayleigh number, which is proportional to the temperature difference ΔT applied across the fluid layer. The diffusive concentration flux driven by the Soret effect (Hurle & Jakeman 1971)

† Permanent address: Universität Bayreuth, D-8580 Bayreuth, Germany.

requires the definition of a second experimentally important parameter: the separation ratio $\psi \equiv -\beta C(1-C)S_T/\alpha$, where C is the mean concentration, S_T is the Soret coefficient, and the expansivities α and β are given by $\alpha \equiv \rho^{-1}\partial\rho/\partial T$ and $\beta \equiv \rho^{-1}\partial\rho/\partial C$ (ρ is the fluid density). In a series of papers on successively better approaches to solving the Boussinesq equations for convection in a binary fluid (Linz & Lücke 1987; Linz *et al.* 1988; Barten *et al.* 1989; Barten, Lücke & Kamps 1990, 1991), it has been shown that the flow fields in travelling-wave convection include a concentration wave in which clockwise-turning and counterclockwise-turning rolls have a different average solute concentration. As was appreciated in the very first paper on travelling-wave convection (Walden *et al.* 1985), the different buoyant forces in rolls with different average concentrations leads to the propagation of the pattern as a whole. As the Rayleigh number is increased, the magnitude of the concentration wave is decreased by mixing in the convective flow, and the propagation velocity decreases. Recent measurement of the propagation velocity in a fluid with $\psi = -0.25$ in a narrow annular container have quantitatively confirmed this model of travelling-wave convection (Ohlsen *et al.* 1990).

While measurements of the propagation velocity of convective rolls indirectly reveal the importance of the concentration wave, a direct measurement of this field has always appeared to be impossible in ethanol/water mixtures. Because of large difference in density between the two component fluids, the buoyancy effects which cause the propagation of convective rolls require roll-to-roll concentration differences which are expected to be so small as to be unobservable, except in their effect on the roll propagation velocity. However, it has recently been realized that a refractive measurement of the concentration wave is indeed possible (Eaton *et al.* 1991). Because of the small Lewis number in this system (the Lewis number L is the ratio of the mass diffusivity D to the thermal diffusivity κ), it is expected that the concentration inside each convective roll is rendered essentially homogeneous by its circulation, so that sharp gradients in concentration only appear at the boundaries between rolls (Bensimon, Pumir & Shraiman 1989). Shadowgraphic flow visualization, in which the image intensity is proportional to the two-dimensional Laplacian of the index of refraction, should be exquisitely sensitive to the sharp index gradients caused by this concentration-field structure. Eaton *et al.* (1991) observed these features in experiments in which travelling-wave convection in a narrow annular container was visualized by shadowgraphy from above. They compared their images with shadowgraphs computed from numerically obtained solutions of the Navier–Stokes equations. They indeed found that the magnitude of the concentration-wave component decreased with increasing Rayleigh number, vanishing as the propagation velocity decreased to zero. At the same time, the phase shift between the concentration and the temperature waves evolved with Rayleigh number in such a way as to restore the fundamental symmetry with respect to reflection about the upflow or downflow roll boundaries that is expected for convective states which do not propagate.

In this paper, we also present visualizations of the concentration wave which accompanies travelling-wave convection in ethanol–water mixtures, this time in a long, rectangular container. A major difference with the work of Eaton *et al.* (1991) is that we employ shadowgraphy *from the side*, using a broad, collimated laser beam which propagates parallel to the roll axes. In this way, we avoid integrating the flow fields in the vertical direction, which would erase the most interesting structure in this two-dimensional flow, namely, the entrainment of solute from the boundary layer by the convective rolls. Even the unprocessed shadowgraph images reveal

qualitative features of the flow which are in exact accord with the numerical computations.

Another important improvement in these experiments is that we have gone beyond comparing experimental shadowgraph images with images obtained by computing the Laplacian of the refractive-index field obtained numerically. Rather, our improved spatial resolution and signal-to-noise level have allowed us to successfully integrate the light intensity in the flow images, so as to obtain the full two-dimensional refractive-index field. Furthermore, because of the differences in spatial structure between the temperature and concentration fields, we have been able to reliably separate their contributions to the refractive index, using image-processing techniques. These results are in good quantitative agreement with theoretical computations. Because our experiment measures not the refractive index itself but only its Laplacian, and that only to within an additive constant which is determined with some imprecision, our image-processing results can be used to reconstruct the true temperature and concentration fields only to within an additive function whose Laplacian is a constant. In our case, this is a quadratic function of the vertical position. In order to fix the three parameters which determine this function, we use a small amount of information from numerically computed concentration and temperature profiles. This allows us to make a full two-dimensional reconstruction of the flow fields that compares quite well with the theoretical results.

While our main aim in this work has been a quantitative comparison of experimental and theoretical concentration fields, the qualitative features of the flow are also extremely interesting. This is especially true in the case of turn-on and turn-off transients. In the former case, the onset of nonlinear convection is marked by the appearance of sharp features caused by the sweeping of solute into the centre of the cell from the boundary layers. As mentioned above, this results in sharp, curved features in the images of equilibrated flows. Images of the transients which precede this equilibration exhibit spiral, vortex-like structures which propagate laterally through the cell, visually revealing the evolution of concentration boundary layers out of the conductive state. Turn-off transients are also quite interesting, because they reveal the presence of two kinds of large-scale currents which are inherent in travelling-wave convection.

This paper is organized in the following manner. We begin by describing the experimental apparatus and the procedure used for visualizing the flow. We then describe in detail the numerical procedures used to process the flow-visualization images and extract the convective temperature and concentration fields. Next, we describe the visualization of convective transients. The final section is a discussion.

2. Apparatus and experimental procedure

These experiments were conducted using a modified version of an apparatus previously used for optical measurements of the Soret coefficient of ethanol/water mixtures (Kolodner, Williams & Moe 1988). The heart of the apparatus is shown in section in figure 1. The convection cell consists of a rectangular quartz frame of inside dimensions $0.30 \times 0.90 \times 6.70$ cm which is clamped between two polished copper plates. In this cell, convective rolls align parallel to the short dimension and propagate parallel to the long dimension. For corrosion protection, the copper has been treated with an aqueous solution of benzotriazole, and all the fill plumbing has been constructed out of Teflon, with ungreased, ethylene-propylene o-ring seals. The

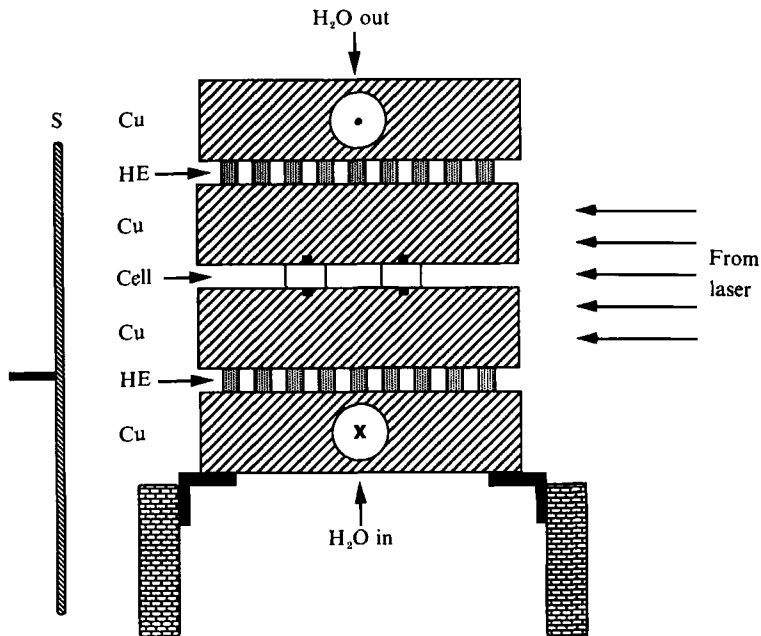


FIGURE 1. Cross-section of the experimental cell. The convecting fluid is contained in a rectangular quartz frame which is clamped between two polished copper blocks (marked 'Cu' in the drawing). These in turn are pressed against thermoelectric heat-exchange units (marked 'HE') which are heat-sunk to the outer, water-cooled copper blocks ('Cu'). To avoid a lateral gradient in Rayleigh number due to warming of the cooling water, the circulation in the heat-sink blocks is counter-current. The cell is illuminated from the right by a broad, collimated laser beam, and the image is formed on the rotating screen (marked 'S') on the left. The cell assembly and the rotating screen are mounted inside an insulated, temperature-regulated copper box for isolation from the environment.

temperature difference applied across the cell is maintained by thermoelectric heat-exchange units above and below the top and bottom copper plates. This central assembly is clamped between water-cooled copper blocks which serve as heat sinks for the thermoelectric units. For thermal isolation from the environment, the cell is surrounded by foam insulation and is placed inside an insulated, water-cooled copper box (not shown in figure 1) whose temperature is maintained at the mean cell temperature.

Temperature regulation of the convection cell is provided by a series of bridge/servo circuits which read the resistances of thermistors embedded in the top and bottom plates of the cell. The temperature of the top plate is held constant to within ± 10 mK by a d.c. bridge circuit which drives the upper heat-exchange units. A second, a.c., bridge circuit drives the lower heat exchangers in response to the temperature difference measured by a pair of thermistors, one of which is embedded in the top plate and the other in the bottom plate. By means of a computer-controlled ratio transformer, this servo system is used to apply a temperature difference across the cell which is stable to within ± 3 mK. This is to be compared with the temperature difference applied across the cell, which ranges from 5 K and 10 K, depending on the parameters of each experiment. A third, d.c., bridge circuit is used to read the resistances in two other thermistors, for calibration and monitoring purposes. A quartz-crystal thermometer probe has been used to provide an absolute calibration of all of the thermistors to within 0.1 K.

The shadowgraphic visualization of the convective flow is accomplished by directing a 9 cm diameter, collimated He–Ne laser beam horizontally through the cell parallel to its short dimension. A refractive image of the convection rolls is formed on a mylar screen located a distance of 5 cm from the centre of the cell. This short distance was used to ensure that the contrast in the image remained linearly related to the refractive-index field in the fluid (Rasenat *et al.* 1989). In order to average out the graininess caused by laser speckle, this screen is spun at about 500 r.p.m. by a small d.c. motor. For most of the experiments reported here, the image of the central 3 cm of the cell (corresponding to approximately 5 pairs of convective rolls) is recorded by a c.c.d.-based video camera whose output is displayed on a monitor and digitized by a frame-grabber board. The spatial resolution of our digitization is quite high: the area of a convective roll is covered by a square mesh of approximately 64×64 pixels. For noise reduction, the frame grabber records the sum of 64 consecutive frames, averaging over a period of approximately two seconds – this is very short compared to the dynamics of the convective patterns. In order to maximize the resolution of the frame grabber, a d.c. bias is subtracted from the image before digitizing, so that the range of contrast in the image fills the entire eight-bit digitization range. The d.c. bias is the same for all images in an experimental run, but its precise value has not been recorded. This will lead to some uncertainty in one of the fit parameters described in the next section.

These experiments were performed using three carefully degassed solutions of ethanol in deionized water, with ethanol concentrations of 8.0%, 10.0%, and 12.0% by weight. By varying the mean temperature in the convection cell between 15 °C and 29 °C, we were able to vary the separation ratio ψ from -0.24 to -0.46 (Kolodner *et al.* 1988). The typical Lewis number and Prandtl numbers in these experiments were 0.008 and 15, respectively.

Our experimental procedure was quite straightforward. Initially, a travelling-wave state was created by setting the Rayleigh number above the onset of convection and waiting until a steady state was established. This typically required a wait of two hours after the onset of convection. Once an accurate and stable measurement of the phase velocity of the convective rolls was made, we acquired a sequence of shadowgraph images for data analysis, and we then changed the Rayleigh number to obtain a new travelling-wave velocity. We typically scanned the Rayleigh number in this way over the entire range from just below the transition Rayleigh number r^* , above which the convective pattern is stationary, down to the saddle-node Rayleigh number r_s , below which a transition back to the conductive state is observed. In addition, most Rayleigh-number scans were repeated with waves travelling in the opposite direction.

As a final remark in this section, we would like to define the notation and dimensionless scalings used in the rest of the paper. As usual, lengths are rendered dimensionless by scaling them with the cell height d , and velocities are scaled with κ/d , where κ is the thermal diffusivity of the fluid. We shall make an exception to this scaling when presenting profiles of the flow fields in the horizontal plane; then, it will be convenient to scale lateral lengths not with the cell height but with the measured wavelength λ of the convective pattern. Temperatures are scaled with the temperature difference ΔT applied across the fluid layer for the individual run under discussion, and concentrations are scaled with $\alpha\Delta T/\beta$ (the expansivities α and β were defined in §1). Locations in the two-dimensional flow field are denoted (x, z) , where x represents the horizontal position and z the vertical position. Finally, we quote reduced Rayleigh numbers computed by dividing the applied temperature difference

ΔT by the temperature difference which corresponds to the onset of steady convection in a laterally infinite geometry for a pure fluid with the same thermal properties as the mixture.

3. Processing of flow-visualization images

3.1. Noise reduction and extraction of the refractive-index field

The first phase of our image-processing procedure consists of shifting and adding images so as to reduce the effects of noise and defects in the visualization. We begin by making a reference image in the absence of convection. Then, after a travelling-wave convective state has been established, we digitize a sequence of 32 images at a sampling rate that is adjusted so that 25 to 30 time steps corresponds to the drift of the pattern by the length of one roll pair. The reference image is subtracted from each of these images. In this way, we obtain images of approximately 150 roll pairs made at different times and places in the cell. By shifting them all to a fixed position and adding, we will obtain an image of a single roll pair with substantially suppressed noise and small-scale image distortions.

Before this averaging is done, we perform a mapping which removes large-scale optical distortions. To measure these, we demodulate at the mean measured wavenumber to compute the wavelength profile $\lambda(x)$ of the periodic function representing the image intensity along the midheight line in each image. We observe that $\lambda(x)$ varies by several percent over the length of the region under examination. This is mostly due to distortions in the lens of the c.c.d. camera; we expect, on the basis of the observations presented by Kolodner (1990), that the influence of the endwalls of the cell on the actual roll wavelength profile does not extend into the central region of the cell which we are examining. Using the technique described by Kolodner & Williams (1990), we map each of the images so that $\lambda(x)$ is rendered flat. We then shift all of the imaged roll pairs to a common location in the image and sum them. The spatial phases of the constituent images are shifted so that the left edge of the sum image corresponds to the location of a downflow roll boundary. One of the results of this shift-and-sum procedure is a precise measurement of the phase velocity of the rolls.

Figure 2 shows the results of this image processing for right-going travelling waves at four different Rayleigh numbers, for $\psi = -0.39$. The left-hand roll is duplicated on the right of the image for clarity. Image (a) was made using fast travelling waves at a Rayleigh number just above the saddle-node point. The sharp, curved features are due to the jump in concentration at the roll boundaries. The central, light 'J'-shaped feature, for example, is caused by ethanol-rich fluid which is swept down and around by a clockwise-rotating convective roll. Images (b-d) in figure 2 were made at successively larger Rayleigh numbers; in particular, image (d) was made using very slowly travelling rolls just below the transition to steady convection. As the Rayleigh number is increased and the propagation of the rolls slows down, the curved parts of the sharp features become less prominent. The physical reasons for this are discussed in §4 below. The reader may note that the dark features in these images are wider than the light features, especially in figure 2(a). This is not an artifact of the processing or of the image reproduction but is due to the concentration dependence of the index of refraction and to the fact that, for this separation ratio, adjacent rolls exhibit a relatively strong concentration contrast. As the separation ratio is made less negative and/or the Rayleigh number is increased, this asymmetry goes away.

Barten *et al.* (1989, 1990) have made several observations about the symmetry of

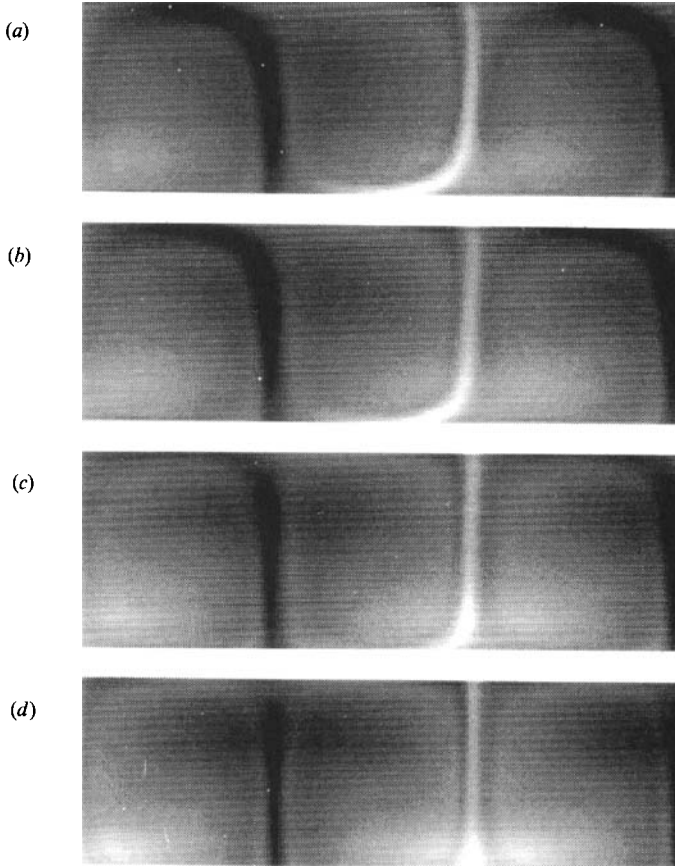


FIGURE 2. Shifted and summed shadowgraph images for right-going travelling waves at four different Rayleigh numbers, for $\psi = -0.39$. (a) $r = 1.339$; (b) 1.385; (c) 1.443; (d) 1.607. The sharp, curved features are due to refraction by sharp concentration gradients at the roll boundaries. The contrast in each image has been separately adjusted to slightly overflow the full grey scale.

one-dimensional patterns of stationary and travelling-wave convection. For example, the temperature and concentration fields in travelling-wave patterns of infinite lateral extent are expected to be antisymmetric with respect to a spatial shift by half a wavelength combined with a reflection through the horizontal midplane. This symmetry is qualitatively evident in all of the images of figure 2. In contrast, steady convective patterns exhibit an additional invariance with respect to reflection through a vertical plane at the position of a downflow or upflow roll boundary. This symmetry is clearly not exhibited by the top images in figure 2, but the deviation from symmetry is seen to decrease as the pattern slows down at higher Rayleigh number. Eaton *et al.* (1991) have shown in detail that the symmetries exhibited by experimental patterns of travelling-wave convection evolve with Rayleigh number essentially as predicted by the numerical calculations.

For each map of the two-dimensional image-intensity field $I(x, z)$, we compute the refractive-index field $n(x, z)$ by numerically solving the Poisson equation: $\nabla^2 n(x, z) = I(x, z)$, using a standard five-point finite-difference approximation. In this integration, we apply periodic boundary conditions in the x -direction and set $n = 0$

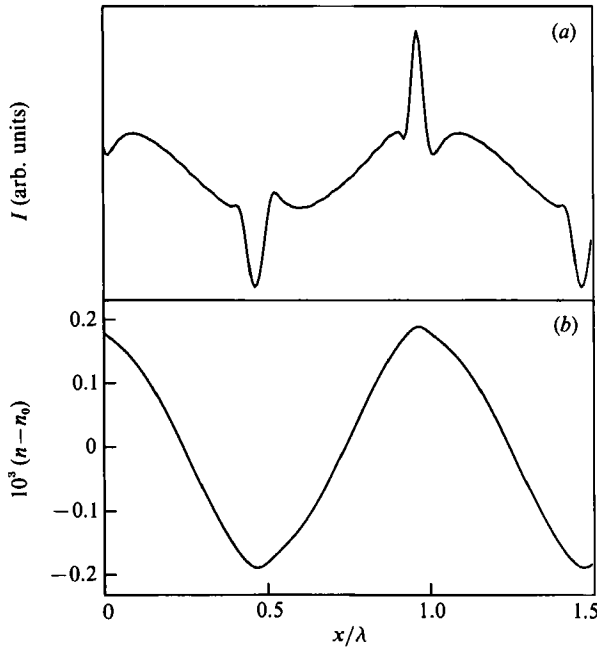


FIGURE 3. (a) Light intensity $I(x)$ vs. lateral position x in the horizontal midplane of an image of right-going travelling waves at $r = 1.399$, with $\psi = -0.39$. The smooth component is caused by the temperature field, and the sharp spikes are caused by the jumps in concentration at the roll boundaries. (b) Refractive index $n(x)$ obtained by numerically integrating the Poisson equation using the intensity field in (a). The sharp features due to the concentration component have been rendered almost invisible by the double integration.

on the upper and lower boundaries $z = (0, 1)$. The conditions imposed at the horizontal surfaces of the cell are, of course, not physically reasonable. However, we are free to add a function of the form $\delta n(x, z) = a + bz + \frac{1}{2}cz^2$ to the computed solution. The constant c is equal to the bias which is subtracted from each image before digitization; as noted above, this parameter is known from our experimental measurements but is somewhat uncertain. The parameters a and b , which are completely undetermined by our experiment, will be obtained by imposing the condition that the experimental refractive-index field must match the numerical results of Barten *et al.* (1989, 1990) at the upper and lower boundaries of the cell. This is discussed in §3.3 below.

3.2. Separation of the temperature and concentration fields in the midplane of the cell

A great deal of insight into the nature of the flow can be obtained if we concentrate briefly on the behaviour of the refractive-index field $n(x)$ as a function of lateral position at midheight in the cell. Figure 3(a) shows the behaviour of the image intensity for a state of right-going travelling waves at $r = 1.399$, in a fluid with $\psi = -0.39$. It is easy to distinguish the smooth, sine-shaped contribution due to the temperature field from the sharp peaks due to the concentration field, just as the sharp features are clearly evidence in the images in figure 2. Eaton *et al.* (1991) analysed data similar to that in figure 3(a) by comparing with the corresponding curves computed from numerical temperature and concentration fields. However, the contribution of the sharp peaks to the refractive-index field obtained by integrating the Poisson equation (figure 3b) consists only of a slight asymmetry which is no longer easy to discern. The problem of extracting the concentration

component $n_C(x)$ from the temperature component $n_T(x)$ is a subtle and serious one which was not addressed by Eaton *et al.*

At first sight, it may appear that this separation is actually impossible. The chief difficulty is already clear from inspection of figure 3(b): $|n_C| \ll |n_T|$. We expect, on the basis both of the theoretical results of Barten *et al.* (1989, 1990) and from the results of successively better analyses of our own data, that $n_T(x)$ should be a smooth function of x , exhibiting a limited spectrum of harmonics of the fundamental spatial frequency, while $n_C(x)$ should exhibit a roughly square-wave shape whose fundamental component is approximately 90° out of phase with $n_T(x)$. The square wave will have substantial energy in high, odd spatial harmonics, but since the dominant spectral weight of both components lies in the fundamental, simple spectral filtering will certainly not suffice to separate them. Likewise, simply computing two quadrature phases of $n(x)$ will not be useful in separating $n_C(x)$ from $n_T(x)$. Because the concentration component is so much smaller in amplitude than the temperature component, small errors in the phase angle will mix a large component of $n_T(x)$ into $n_C(x)$.

Despite these considerations, we have been able to reliably extract the concentration component by using a fitting procedure that exploits not just its phase and harmonic structure, but also its full square-wave shape. In our fit, the temperature component is modelled by the sum of a sine wave at the fundamental wavenumber and its first two harmonics:

$$n_T(x) = n_{T_1} \sin(kx + \phi_T) + n_{T_2} \sin(2kx + \phi_T) + n_{T_3} \sin(3kx + \phi_T). \quad (1)$$

Note that the phases of the harmonics of $n_T(x)$ are locked to that of the fundamental. The concentration component is modelled by a function f which explicitly exhibits the shape of a square wave with finite-width transitions:

$$n_C(x) = n_{C_1} f(\delta, kx + \phi_C), \quad (2)$$

where $f(\delta, kx + \phi_C)$ is a clipped sine wave or 'trapezoid wave' of unit amplitude:

$$f(\delta, y) = \begin{cases} 1, & \delta \sin y > 1 \\ \delta \sin y, & |\delta \sin y| < 1 \\ -1, & \delta \sin y < -1. \end{cases} \quad (3)$$

The constant δ parametrizes the width of the transitions in the 'trapezoid wave' function $f(\delta, y)$. We fit the refractive-index profile $n(x)$ to the sum of the concentration and temperature components as just described, plus an offset n_0 ,

$$n(x) = n_0 + n_T(x) + n_C(x), \quad (4)$$

using a nonlinear-least-squares algorithm which varies the eight parameters n_0 , n_{T_1} , n_{T_2} , n_{T_3} , n_{C_1} , ϕ_T , ϕ_C , and δ . In figures 4(a) and 4(b), the smooth curves show the temperature field $T(x) = (\Delta T \partial n / \partial T)^{-1} n_T(x)$, where the factor $\partial n / \partial T$ is evaluated at the mean temperature T_0 and concentration C_0 at the midplane of the cell (Kolodner *et al.* 1988), and $n_T(x)$ is evaluated using the functional form in (1) and the fit parameters found for a right-going wave with phase velocity $v_{ph} = 0.916$ (figure 4a) and for a left-going wave with $v_{ph} = -0.788$ (figure 4b). The trapezoid-wave-shaped curves represent the concentration field $C(x) = (\partial n / \partial C)^{-1} n_C(x)$, scaled by $\alpha \Delta T / \beta$. In computing $C(x)$, instead of the function in (2) and (3) we used the difference $n(x) - n_0 - n_T(x)$ computed with the fitted results for n_0 and $n_T(x)$. The function $f(\delta, y)$ is not proposed as the correct shape for $n_C(x)$; it is merely used as tool for forcing the fit to correctly separate the smoothly varying components of $n(x)$ from the concentration component. These curves show that the full refractive-index field does

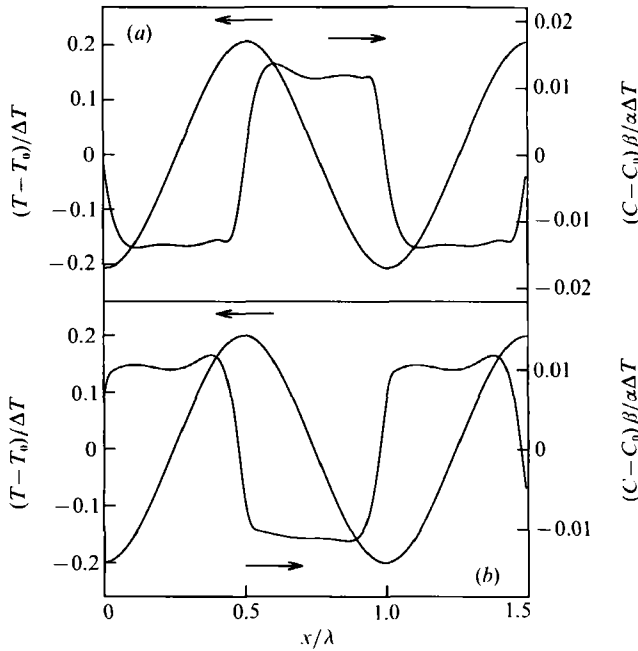


FIGURE 4. Scaled temperature and concentration fields as functions of lateral position x at mid-height in the cell, as obtained by integrating the Poisson equation for: (a) a state of right-going and (b) a state of left-going travelling waves at $r = 1.399$. While the Rayleigh number was nominally identical for these two states, their phase velocities are slightly different. The separation ratio was $\psi = -0.39$.

indeed consist of the sum of a smooth component, which we attribute to the temperature field, and a trapezoid-wave-shaped component, which we attribute to the concentration field.

There are several ways to assess whether this decomposition into differently shaped waves does reliably determine the true temperature and concentration fields. First, we can ask whether changes in the fit procedure introduce systematic errors into the extracted concentration field. Our basic observations concern the strength of the harmonic components of the refractive-index field. For all of our fits at midheight, we find $n_{T_2} \ll n_{C_1} \ll n_{T_1}$ and $n_{T_3} < \frac{1}{2}n_{C_1}$. Thus, the second-harmonic component is always negligible, and the third-harmonic component is small but not negligible compared to the concentration component. The most important systematic error we can conceive of in our procedure is that the third harmonic should really be attributed to the concentration component rather than to the temperature component. What error results if this is done? We have answered this question by redoing all of our fits using only the fundamental component in (1). The resulting curves for $n_C(x) \equiv n(x) - n_0 - n_T(x)$ exhibit wiggles due to the added third-harmonic component, but these have an amplitude which is only 50% of that of the fundamental in the worst case. Importantly, the fit parameter n_{C_1} is unaffected by this change – by choosing the flat-topped fit function in (3), we have averaged out the added wiggles.

Having performed one test of the effect of systematic errors in our fit procedure, we next evaluate the random errors by studying the behaviour of the fitted parameters as the Rayleigh number and separation ratio are varied in independent experiments. Comparison with temperature and concentration fields derived from

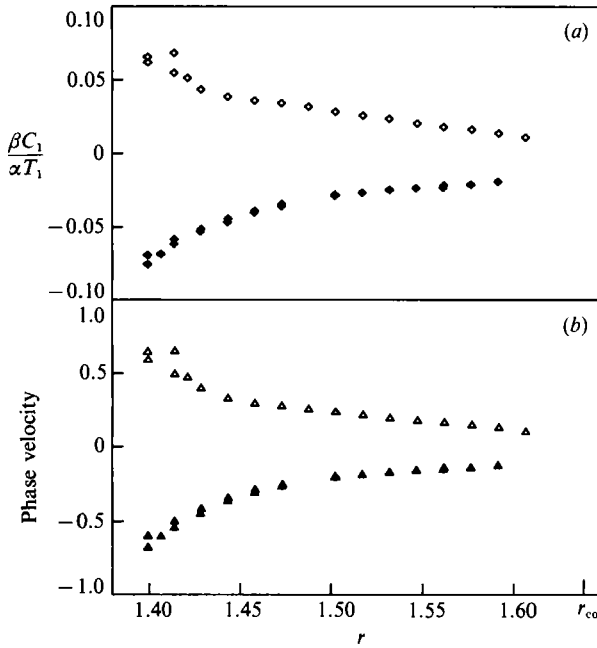


FIGURE 5. (a) The dimensionless ratio of the amplitudes of the fundamental components of the concentration and temperature fields is shown as a function of reduced Rayleigh number, for a series of experiments at $\psi = -0.39$. Open and closed symbols represent data for states of oppositely propagating travelling waves. (b) Dimensionless phase velocity *vs.* reduced Rayleigh number for the same experiments. The amplitude ratio and the phase velocity appear to exhibit the same dependence on Rayleigh number.

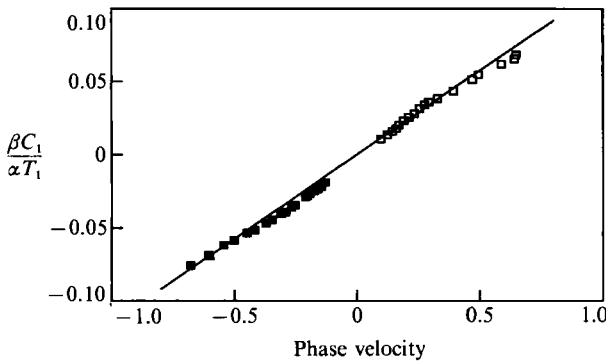


FIGURE 6. The amplitude ratio in figure 5 (a) is plotted against the phase velocity in figure 5 (b). The two measured parameters are very accurately proportional, as shown by the straight line, which is a fit that passes through the origin.

numerical solutions of the Navier–Stokes equations is also useful, and W. Barten has provided us with twenty-one such data sets, computed at various Rayleigh numbers for $\psi = -0.25$. Figure 5(a) shows the dependence on the Rayleigh number of the amplitude of the concentration field, $C_1 \equiv (\partial n / \partial C)^{-1} n_{C_1}$, normalized by the amplitude $T_1 \equiv (\partial n / \partial T)^{-1} n_{T_1}$ of the fundamental component of the temperature field. The derivatives of the refractive index are again evaluated at the mean temperature and concentration at midheight in the cell. As shown by the open and closed symbols, this amplitude has opposite signs for left- and right-going travelling waves. These measurements exhibit some scatter at low Rayleigh numbers which may have been

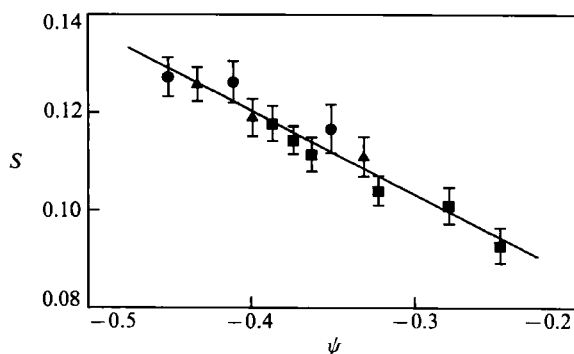


FIGURE 7. The constant of proportionality s determined from data like those in figures 5 and 6 is shown as a function of separation ratio ψ . Circles: 8.0 wt-% solution; triangles: 10.0 wt-% solution; squares: 12.0 wt-% solution. The straight line is a least-squares fit.

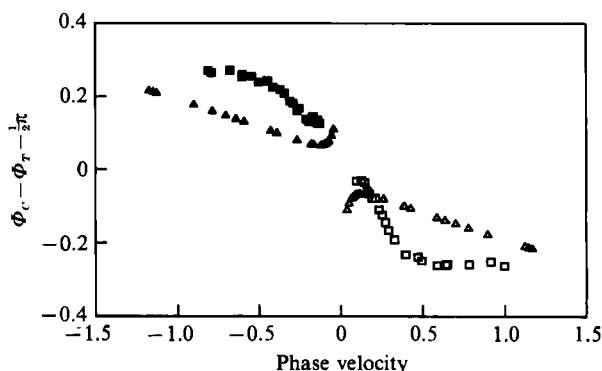


FIGURE 8. The square symbols show the phase angle $\phi_C - \phi_T - \frac{1}{2}\pi$ of the concentration wave with respect to the temperature wave as a function of the phase velocity of the travelling waves for $\psi = -0.39$. The triangles show the phase difference between the fundamental components of the concentration and temperature waves computed numerically for $\psi = -0.25$ by W. Barten. Open and closed symbols represent oppositely propagating travelling waves.

caused by incorrect measurement or recording of the Rayleigh number. Remarkably, however, the travelling-wave phase velocity v_{ph} (figure 5*b*) exhibits practically identical behaviour, including the scatter. Indeed, as shown in figure 6, these two measured parameters are accurately proportional, a fact which, as far as we are aware, has not been noticed previously. As shown in figure 7, the constant of proportionality $s \equiv \beta C_1 / \alpha v_{ph} T_1$ is a linear function of the separation ratio. The straight line in figure 7 is a least-squares fit: $s = d\psi + e$, with $d = -0.171 \pm 0.013$ and $e = 0.052 \pm 0.005$. The numerical data for $\psi = -0.25$ also exhibit a proportionality between C_1 and T_1 , with a proportionality constant $s = 0.089 \pm 0.003$. This agrees with our measurement of $s = 0.092 \pm 0.004$ at $\psi = -0.25$. This close agreement, combined with the corroboration of the numerical results by the phase-velocity measurements of Ohlsen *et al.* (1990), is a strong indication that our separation of the concentration and temperature waves is reliable, and that the theory makes correct predictions about the strength and systematic behaviour of the concentration field.

In figure 8, the phase difference between the concentration and temperature waves, $\phi_C - \phi_T - \frac{1}{2}\pi$, is shown as a function of the travelling-wave phase velocity for $\psi = -0.39$. As in previous figures, open and closed squares represent data for right- and left-travelling waves, respectively. The sign convention we employ in our fit procedure is that the two directions of propagation differ in the sign of the

concentration field. This implies that, as a function of phase velocity, the phase angle $\phi_C - \phi_T$ should be antisymmetric about $\frac{1}{2}\pi$ (cf. figures 4(a) and 4(b), which show the flow fields for left- and right-going states at nearly the same phase velocity). The experimental points are indeed nearly exactly antisymmetric about $\frac{1}{2}\pi$ and exhibit a low level of scatter. At high phase velocity, the phase angle is seen to saturate at a value of about 0.6π , as can be confirmed approximately by inspecting figure 4. The phase lag exhibited by the numerically computed flow fields, as represented by the open and closed triangles in figure 8, agrees with the experimental phase angle to within about 0.1 rad and appears to approach it at high phase velocity.

Our procedure for separating the fundamental components of the temperature and concentration waves rests on three physically reasonable but *ad hoc* assumptions. First, we have assumed that the concentration field exhibits a flat-topped shape because of the strong mixing inside the individual convective rolls. Second, we have assumed that the fourth and higher harmonics of the refractive-index field belong to the concentration field. These assumptions are supported by the numerical data of Barten *et al.* (1989, 1990), in which the concentration field does exhibit a flat-topped shape, and in which the fourth and high harmonics of both fields are negligible. Third, we have assumed that the first three harmonics of the temperature field have the same phase. This behaviour is not exhibited by the numerical data, but our test of reanalysing the data without including the second and third temperature harmonics showed that the quantitative results are little affected by this assumption. Eaton *et al.* (1991) have observed that the third harmonic of the temperature field is weaker in experiments in a narrow annular container than the numerical calculations predict, and they suggest that this represents a suppression by the sidewalls of the cell. While our cell is wider than that of Eaton *et al.*, this conjecture may be the key to the unimportance of the phase of the third temperature harmonic to our analysis. With these assumptions, our fit procedure produces a robust set of fit parameters which are consistent with the numerical computations.

3.3. Reconstruction of the full two-dimensional flow fields

The procedure used to separate the temperature and concentration components of the refractive index at the cell midplane can be performed for each of the other 63 horizontal lines of data in our flow-visualization images, with two modifications. In the midplane of the cell, the concentration profiles were found to exhibit the shape of a trapezoid wave with a 50% duty cycle (a 'symmetric' waveform). Indeed, this symmetry is to be expected for a system which exhibits a symmetry involving reflection through the midplane. However, as can be seen in figure 2(a, b) the shape of the concentration profiles at other vertical positions in the cell can be expected to be asymmetric – i.e. to exhibit a duty cycle which differs from 50%. This asymmetry is associated with even harmonics of the fundamental wavenumber. Including the harmonic terms in (1) would therefore incorrectly mix components of the concentration wave into the temperature wave, and so we have dropped them. In this way, we sacrifice the ability to learn anything about the third harmonic of the temperature wave, but we already know from the tests made on the fits to data at midheight that this procedure need not affect the accuracy with which we can measure the amplitude and phase of the fundamental component of the concentration wave. However, since we are now fitting an asymmetric concentration wave with the symmetric function defined in (3), it will no longer be correct to quote the fit parameter n_{C_1} as its amplitude. Instead, as was done in the previous section, we used the fitted offset n_0 and temperature component n_T to compute the concentration

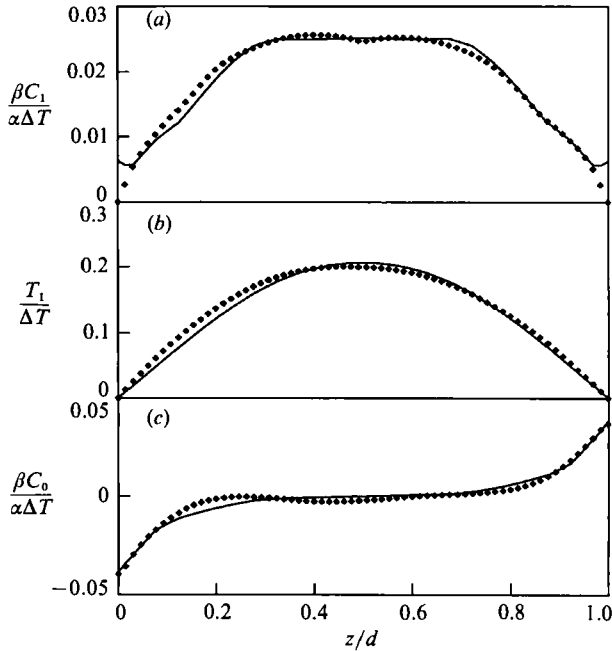


FIGURE 9. The dimensionless concentration and temperature field amplitudes (a) C_1 , (b) T_1 , and (c) C_0 are plotted as functions of height z in the experimental cell. Diamonds represent the parameters of fits to the experimental data for $r = 1.287$ and $\psi = -0.25$. For these data, the measured phase velocity was $v_{\text{ph}} = 0.728$. The solid curves were interpolated to this value of v_{ph} ($r = 1.26$) using theoretical profiles computed for $\psi = -0.25$ by W. Barten.

component $n_C(x, z) \equiv n(x, z) - n_0(z) - n_T(x, z)$, and we measure its peak-to-peak amplitude $C_1(z)$ independently of the fit procedure by measuring the difference between its asymmetric flat extrema. The second modification to the fit procedure is that we fix the transition-width parameter δ in (3) at the value determined by the fit at midheight. Having distorted the higher-harmonic components of $n_C(x, z)$ by using a symmetric fit function, it would be pointless to try to improve the fit by varying a parameter which chiefly affects those higher harmonics.

The discrete symbols in figures 9(a) and 9(b) show the fit results for the z -dependence of the amplitudes $C_1(z)$ and $T_1(z)$ for a state of left-going waves at $r = 1.287$ and $\psi = -0.25$. Both fields drop to zero at the horizontal boundaries of the cell. While the temperature field exhibits a smooth, sine-like profile, the concentration field exhibits a broad plateau in the centre of the cell. The smooth curves in the figures have been interpolated from the numerically computed flow fields of W. Barten. In comparing the numerical and experimental results, it must be kept in mind that the width of our experimental cell, $\Gamma = 3.0$, has a poorly known effect on the experimental measurements. We know from our own unpublished experiments that the onset Rayleigh number for the linear oscillatory instability is suppressed by 2.2% in our cell over the value computed for a laterally infinite layer. As noted by Ohlsen *et al.* (1990), the Rayleigh-number scale for nonlinear states is also affected by the cell width, but this effect is not understood quantitatively. Furthermore, the scatter in figure 5 has already made us suspect that the measured Rayleigh number is not always the most reliable index of the convective state. Therefore, rather than comparing numerical and experimental results at the same Rayleigh number, we have elected to make comparisons based on matched phase velocities. Because of the observed proportionality between v_{ph} and the ratio C_1/T_1 shown in figures 6 and 7,

this is equivalent to assuring that the *peaks* of the measured concentration and temperature profiles at midheight match the numerical computations. The real comparison between computation and measurement consists of asking whether the *shapes* of the computed and measured profiles also agree for all heights z in the cell.

The numerical concentration and temperature profiles, shown as the solid curves in figures 9(a) and 9(b), give part of the answer to this question. The computed concentration profile in figure 9(a) matches the experimental points quite well, except at the very top and bottom of the cell, where the experimental curves vanish. This small discrepancy is caused by the imposition of constant-refractive-index boundary conditions in the integration of the Poisson equation. This procedure is unphysical. The true boundary conditions consist of a constraint on a linear combination of $C_1(z)$ and $T_1(z)$ (the equivalent of (6) below). It is not possible to impose this constraint in our data analysis, because it would require an *a priori* separation of the fundamental component of the refractive-index field into its temperature and concentration components. However, judging from figure 9(a), this error has minor consequences. The experimental temperature profile in figure 9(b) shows a slight asymmetry with respect to the computed profile. This is a consistent feature in all of our data. The temperature dependence of the refractive index has been taken account of in this analysis, and the concentration variation at this value of ψ is not large enough for this to be purely an optical artifact. This asymmetry may therefore represent a slight non-Boussinesq effect. Finally, it is useful to note that, for the four experimental data sets for which a direct comparison with theory is possible, the average ratio of the theoretical and experimental Rayleigh numbers is 1.01 ± 0.02 . Forcing the peaks of the fundamental-component profiles to match at midheight did not require us to manipulate the Rayleigh numbers unreasonably.

The evolution of the shape of the concentration profile $C_1(z)$ with Rayleigh number is illustrated in figure 10(a). These profiles, which correspond to the four images in figure 2 at $\psi = -0.39$, are spaced approximately equally in phase velocity. As the Rayleigh number is increased, the peak amplitude of the concentration profile decreases, and the central plateau broadens, corresponding to a decrease in the thickness in the concentration boundary layers at the top and bottom surfaces of the cell. Both of these effects can be attributed to the enhanced mixing by the convective flow at higher Rayleigh number. The dips in the concentration profiles at midheight, as well as the lack of symmetry about the midplane seen at the highest Rayleigh number in figure 10(a), probably represent systematic errors in our data analysis rather than true features of the concentration fields. The curves in figure 10(b) are derived from the numerically computed concentration fields for $\psi = -0.25$ provided by W. Barten. They have been interpolated from the original data to equally spaced values of the phase velocity to match the conditions in figure 10(a). Because of the difference in separation ratio, the computed and measured concentration profiles cannot be expected to agree in detail. Nonetheless, the main features just noted – the broadening and weakening of the plateau in the centre of the cell as the Rayleigh number is increased – are exhibited by both the numerical and experimental profiles.

Having found that the fundamental components of the experimental temperature and concentration fields match the numerically computed fields quite well, we now turn our attention to the zero-spatial-frequency (or ‘d.c.’) components $T_0(z)$ and $C_0(z)$. As we pointed out above, our experiments do not determine these fields unambiguously. Rather, we measure the d.c. component of the total refractive-index field, and only to within an additive quadratic function of z . The three parameters of this function can in principle be determined by forcing the experimental

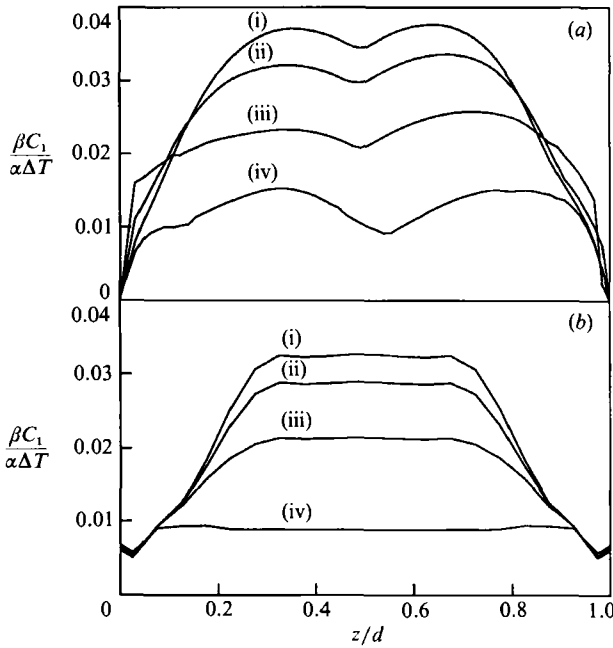


FIGURE 10. (a) Experimentally measured profiles $C_1(z)$ of the fundamental concentration component are shown for various Rayleigh numbers at $\psi = -0.39$. Curve (i) $r = 1.339$, (ii) $r = 1.385$, (iii) $r = 1.443$, (iv) $r = 1.607$. These profiles were computed from the images in figure 2 and are separated by approximately equal differences in phase velocity. (b) Theoretical concentration profiles for $\psi = -0.25$, interpolated to equally spaced phase velocities so as to match the curves in (a). Curve (i) $r = 1.22$, (ii) $r = 1.24$, (iii) $r = 1.28$, (iv) $r = 1.43$.

temperature and concentration fields to obey the same boundary conditions as the computed fields. However, contrary to the case for the fundamental-wavenumber components, which differ strongly in shape, there does not seem to be a way to separate the d.c. concentration and temperature fields. Therefore, we have chosen to concentrate all our uncertainty into $C_0(z)$ by setting the temperature field equal to the theoretical profile $T_{0,\text{th}}(z)$ and putting

$$C_0(z) = (\partial n / \partial C)^{-1} [n_0(z) - (\partial n / \partial T) T_{0,\text{th}}(z)] + a + bz + \frac{1}{2}cz^2. \quad (5)$$

The free parameters a , b and c should in principle be determined by the requirements that the average of $C_0(z)$ over z must be 0 (we subtract out the mean concentration), and that the diffusive component of the concentration flux must vanish at the upper and lower boundaries of the cell, where the convective part of the flux vanishes:

$$\partial C_0 / \partial z + S_T C_0 (1 - C_0) \partial T_0 / \partial z = 0, \quad z = (0, 1). \quad (6)$$

(Here, S_T is the Soret coefficient; indeed, this equation for the concentration flux is the definition of S_T .) We have found that the noise in the experimental data is too large to allow an accurate calculation of the derivatives in (6). Instead, therefore, we have adjusted the parameters a , b and c by applying the *ad hoc* condition that the component of $C_0(z)$ that is antisymmetric with respect to reflection about the cell midplane should be minimized. For the numerically computed concentration field, this antisymmetric component is observed to vanish. The data in figure 9(c) show a typical result. With three adjustable parameters, it is hardly surprising that the experimental profile can be made to match the numerical curve quite well. To put this result in perspective, two comments are in order. First, the fit parameter c is

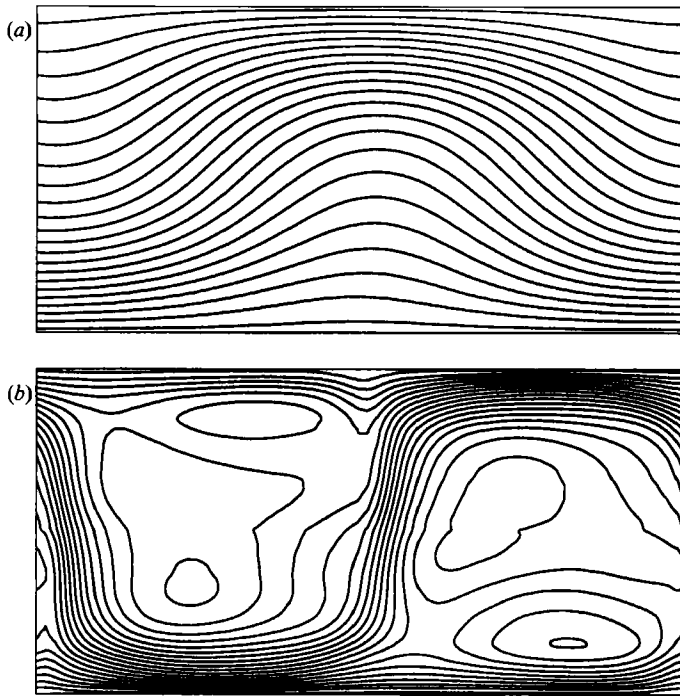


FIGURE 11. Two-dimensional plots of lines of (a) equal temperature and (b) equal concentration for a single pair of convective rolls as reconstructed from data taken at $r = 1.287$ in a fluid with $\psi = -0.25$. In (a), the temperature contours are spaced by $\delta T = 0.161$ °C, and the temperature difference applied across the cell is $\Delta T = 3.698$ °C. In (b), the concentration contours are spaced by $\delta C = 3.04 \times 10^{-4}$, corresponding to a dimensionless concentration difference $\beta \delta C / \alpha \Delta T = 0.00408$.

observed to match our experimentally measured image-intensity offset to within our experimental uncertainty. Second, it should be appreciated that the typical difference between the numerical and experimental profiles for $C_0(z)$ represent typically 1% of our measured refractive-index field, a tiny fraction of the total measured signal.

With the results of the numerical procedures just described, we can now reconstruct the full, two-dimensional concentration and temperature fields. An example is given in figure 11, where the lines of equal temperature (figure 11a) and equal concentration (figure 11b) are shown for a single roll pair in a left-going state at $r = 1.287$, with $\psi = -0.25$. Because our fit and reconstruction procedures have put all the noise into the concentration field, the temperature field in figure 11(a) is smooth and noise-free. The equal-concentration contours in figure 11(b) show the different concentrations in adjacent rolls and the sharp jumps in concentration at the roll boundaries. Each roll exhibits two weak extrema in the concentration, separated by a nearly horizontal line of local minimum. The structure corresponds to the dip in the concentration profile $C_1(z)$ plotted in figure 10(a). This is the principal difference between our reconstruction and the numerical computation, which predicts an essentially uniform concentration within each roll.

4. Visualizations of transient flow fields

The results presented so far in this paper have come from the analysis of carefully prepared, steady states of travelling-wave convection. We have exploited the spatial and temporal periodicity of the data for noise reduction, and this has allowed us to

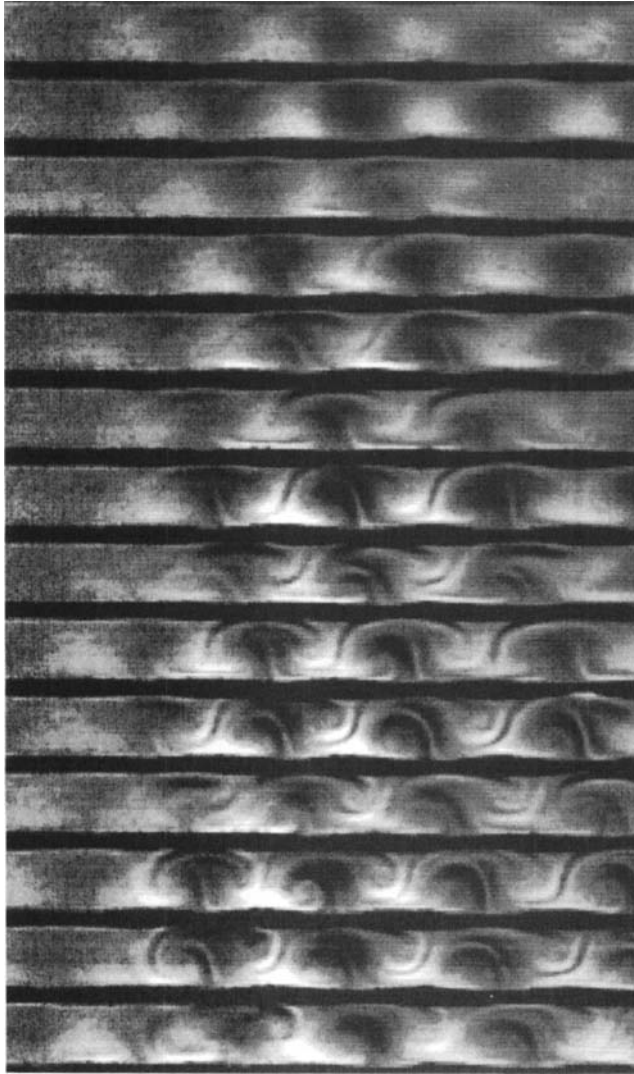


FIGURE 12. Sequence of shadowgraph images taken every 5 s, starting at the top and proceeding downwards in time. The first image was made 160 s after the Rayleigh number was increased from $r = 1.592$ to 1.730, with $\psi = -0.45$. The initial stage of this transient consists of linear waves which cause the weak, periodic contrast in the first two images. The lower images show the 'spatial collapse' by which this pattern of linear waves forms a spatially confined nonlinear pattern before filling the entire cell with rolls. In this stage of evolution, the multiple thread-like curves which mark the roll boundaries are evidence that the rolls rock back and forth repeatedly rather than circulating continuously in one direction.

make precise quantitative analyses of the data. We have also conducted many experiments on transient flows. In such cases, we are less able to use symmetries for noise reduction, but a great deal of useful qualitative information is nonetheless revealed by such observations.

Figure 12 is a sequence of shadowgraph images taken from one such transient experiment. In this run, the Rayleigh number was jumped from just below the onset of convection ($r = 1.592$) to somewhat above onset ($r = 1.730$). Onset transients can

be quite complex in this system, even in this one-dimensional geometry (Kolodner *et al.* 1987; Moses, Fineberg & Steinberg 1987; Steinberg, Moses & Fineberg 1987). However, the jump in Rayleigh number is small enough that a spatially coherent flow persists for a substantial length of time, and the subsequent 'spatial collapse' caused by nonlinearities occurs gradually (see especially figure 2 of Steinberg *et al.* 1987). The first phase of the onset transient consists of the exponential growth of linear travelling waves (Kolodner *et al.* 1986; Surko & Kolodner 1987) which are responsible for the contrast in the first two images in figure 12. Because the linear state consists of an infinitesimal rocking back and forth of periodically arrayed regions rather than fully 'overturning' or continuously circulating rolls, the shadowgraph image in this stage consists of a weak, smooth, periodic pattern of light intensity. As the amplitude of the rocking motion increases (middle images in figure 12), it begins to cause finite-amplitude disturbances to the diffusive concentration field, and this leads to thread-like structures where sharp concentration gradients mark the flow. In addition, this region of finite amplitude begins to be spatially confined – a nearly motionless front separating finite-amplitude motions from nearly quiescent fluid is visible on the left of the bottom images in figure 12, and a corresponding front is expanding beyond the right edge of the images. The persistence of several dark and light bands at each roll boundary in the bottom images in figure 12 indicates that the rolls are still rocking back and forth and have not yet begun to turn continuously in one direction.

The sequence of images in figure 13 is taken from another transient in which convection was triggered less abruptly by making a somewhat smaller jump in Rayleigh number: from $r = 1.591$ to $r = 1.687$. In this run, the flow evolves directly to fully overturning rolls marked by continuous, multiple-turn spiral features rather than the thread-like features in figure 12. We suggest that the appearance of overturning rolls in figure 13 represents the nonlinear evolution of pure travelling waves in the linear state which is first triggered by the jump in Rayleigh number. In contrast, the rocking back and forth visible in figure 12 is caused by the presence of a substantial standing-wave component in the linear waves. Our reasoning is as follows. The smaller jump in Rayleigh number in the run in figure 13 allows the transition to nonlinear convection to be preceded by a substantial period of linear growth. During this phase, the linear waves evolve towards the equilibrium pattern seen exactly at onset, in which left-going waves dominate on the left of the cell and right-going waves dominate on the right of the cell. (Kolodner *et al.* 1986). The nonlinear state seen in figure 13 shows the same pattern of wave directions. In the run of figure 12, however, there is much less time for this linear evolution, and linear waves propagating in both directions are found everywhere in the cell, leading to a pattern with a substantial standing-wave component. In the centre of the cell, as visualized in figure 12, even though the right-going linear wave component is dominant, it is accompanied by a substantial left-going component. The standing-wave component in the linear wave pattern grows into nonlinear rolls which rock back and forth before the linear wave pattern can evolve into the more equilibrated pattern seen in figure 13.

It is instructive to follow the evolution of an individual roll in figure 13. For example, a weak, dark feature is just becoming visible on the bottom surface of the cell, just to the left of the middle of the second image from the top. This feature is caused by a warm plume of ethanol-poor fluid which is rising from the bottom surface. As time progresses, this plume rises and curls continuously around in the clockwise direction without changing direction, forming a spiral with several turns

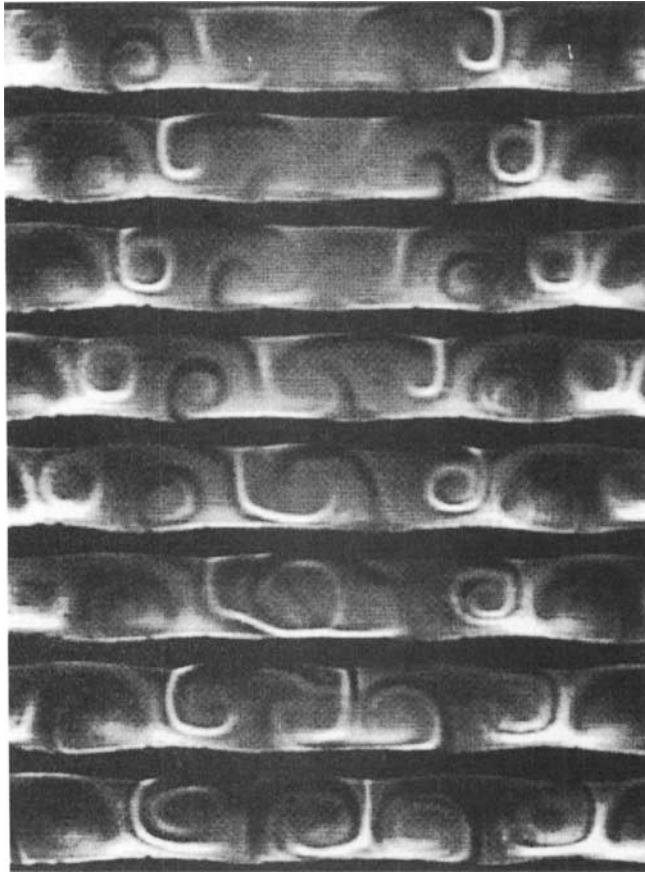


FIGURE 13. Sequence of shadowgraph images taken during a turn-on transient with $\psi = -0.45$ which is less abrupt than that shown in figure 12. The time step between images was 10 s. In the linear phase of this run, the waves on the right side of the cell were dominantly right-going, and those on the left side of the cell were dominantly left-going. These linear waves evolved directly into 'overturning' rolls, which are marked by continuous light or dark spirals, as opposed to the multiple thread-like features in figure 12. This transient also exhibited a spatiotemporal defect, as the rolls are seen to propagate outwards from the centre of the image.

as its position drifts to the left. The spiral structure is gradually erased by diffusion, so that a nearly homogeneous roll has been formed by the time the plume has drifted to the left edge of the image in the bottom frame. Several other similar evolutions are evident in this picture. These transient images directly show the formation of the concentration boundary layers which is associated with fully equilibrated travelling-wave states.

This sequence of images also gives some insight into the behaviour of defects in this system. The second roll from the left in the bottom image contains ethanol-rich fluid swept down from the upper boundary layer and is drifting to the left. Its neighbour to the right, however, exhibits both dark and light 'J'-shaped features, and it is drifting very slowly to the right. The separation of the two rolls will eventually create an unstable situation which can be resolved in one of two ways. First, two new rolls can be nucleated, forming a spatiotemporal dislocation of the type visualized by Bensimon *et al.* (1990). This class of defect also includes the mutual annihilation that can occur when two neighbouring rolls move towards one another. Second, one of the

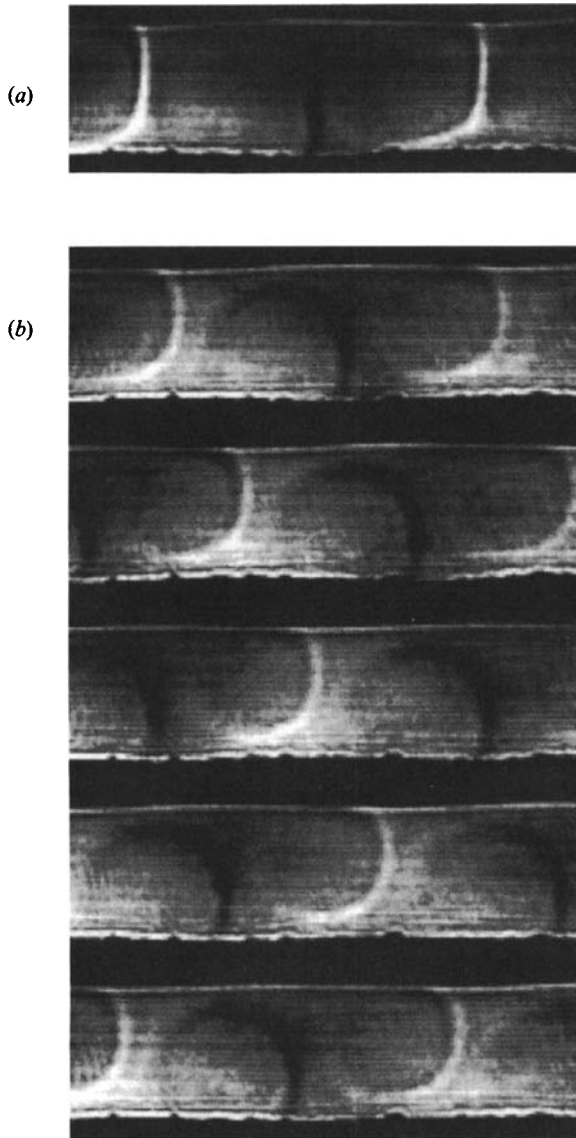


FIGURE 14. (a) One image from an equilibrated state of right-going travelling waves with $\psi = -0.39$, at $r = 1.326$, just above the saddle node. (b) Transient state of travelling waves seen after the Rayleigh number is dropped to $r = 1.241$, just below the saddle node. Before the rolls decay away, they speed up substantially. In order to maintain the balance between the large-scale backflow and the lateral flux of fluid travelling with the travelling waves, the rolls shrink in size, leaving a visible open path for the backflow. The images were made every 20 s, starting at the top and proceeding downwards in time.

rolls can reverse its direction of drift and follow the other. However, this would require the roll which reverses its drift direction to exchange ethanol with its neighbours, and this is a slow, diffusive process. Thus, it is to be expected that the evolution of such situations takes the form either of abrupt spatiotemporal dislocations or very slow reversals of drift direction. This is indeed what is observed in experiments – see, for example, figure 9 of Bensimon *et al.* (1990).

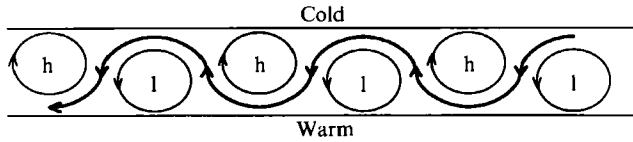


FIGURE 15. Sketch of the flow in figure 14(b), shown in a comoving frame. In a pattern of travelling waves, the fluid is separated into a component which is trapped in the rolls and moves with them at the phase velocity (contained inside the closed curves) and a balancing backflow component which threads over and under the rolls in the opposite direction (heavy open curve). In a pattern which travels to the right, clockwise-circulating rolls have higher ethanol concentration ('h') than average, and counterclockwise rolls have lower concentration ('l').

Figures 14(a) and 14(b) illustrate a phenomenon which is of great importance in steady, nonlinear travelling-wave convection but which is most directly observed in a turn-off transient. In figure 14(a), we show a well-equilibrated state of fast travelling waves just above the saddle node, with $\psi = -0.39$. Figure 14(b) shows the transient pattern created when the Rayleigh number is dropped to just below the saddle node. In the long run, the convection pattern decays away, but its phase velocity increases substantially before it does so. In this way, we can create convective patterns which propagate much more rapidly than they do under stable conditions. In figure 14(b), it is evident that the fast rolls have decreased substantially in size. The ethanol-poor, counterclockwise-circulating rolls remain closer to the lower cell boundary, leaving an open space above them, and the ethanol-rich, clockwise-circulating rolls have pulled up against the upper cell boundary.

The behaviour shown in figure 14(b) is evidence of the existence of a large-scale, two-component current in this system. Linz *et al.* (1988) and Barten *et al.* (1989, 1990) first pointed out, on the basis first of a Galerkin-approximation calculation and then using full numerical integrations of the Navier–Stokes equations, that, when viewed in a comoving frame, a pattern of travelling rolls exhibits separatrices, roughly equivalent to the roll boundaries, which separate two components of the fluid. One component is trapped within the convective rolls and moves with them at their phase velocity. In a closed system, this mass flux must be balanced by a second component, a backflow which threads over and under the rolls in the direction opposite to the wave propagation. As the phase velocity is increased, the rolls would transport a greater flux if their size remained the same; thus, they must shrink and allow a greater backflow. The sketch in figure 15 shows the flow in figure 14(b) interpreted in these terms. Our experiments reveal that, in order to accommodate the increased backflow, the ethanol-rich rolls retract towards the upper cell boundary, while the ethanol-poor rolls move towards the lower boundary.

Moses & Steinberg (1988, 1989) gave evidence of this large-scale current in a series of beautiful experiments on weakly nonlinear travelling-wave convection in which a small fluid element was marked by excitation of dissolved photochromic dye. Viewing the flow from above, and thus integrating over the height of the cell, they observed that the dyed fluid split into two components, one travelling with the convective rolls at their phase velocity, and the other drifting in the opposite direction, at a velocity which depends on the ratio of the phase velocity to the velocity of circulation inside a roll. A simple Lagrangian calculation of the flow exhibited the separation of the fluid into two oppositely drifting components which matched the experimental observations. The behaviour of their model is just that shown in figures 14(b) and 15.

Another important large-scale current associated with travelling-wave convection

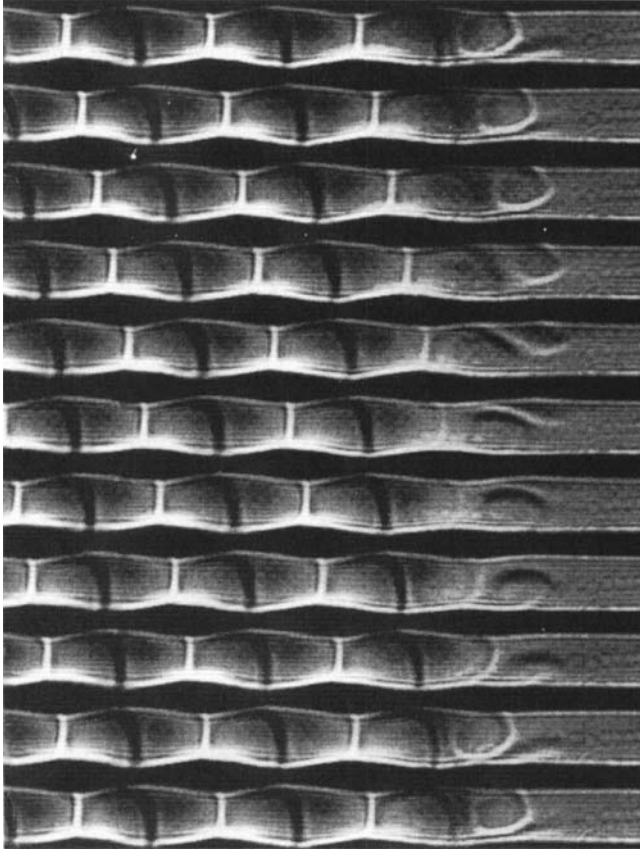


FIGURE 16. 'Neutrally-stable front' between a state of right-going rolls on the left and a quiescent state on the right, made at $r = 1.311$ and $\psi = -0.39$. Time starts at the top and proceeds downwards at a sampling rate of one image every 20 s. The front is marked during the first half of the sequence by a light-outlined, clockwise-circulating roll of ethanol-rich fluid which gradually shrinks as it moves upwards into the top half of the fluid layer. During the second half of the sequence, a dark-outlined, counterclockwise-circulating roll of ethanol-poor fluid shrinks into the lower half of the fluid layer. In order to enhance the contrast in these images, the screen of the optical system was pulled back quite a distance from the cell. The increased path length caused the outline of the upper and lower cell boundaries to be distorted.

is illustrated in the transient flow of figure 16. This is an image of a 'neutrally-stable front' (Kolodner 1990) which separates a region of slow travelling-wave convection from a non-convecting region. In this state, the front propagates through the system, leading to a transition either to a state in which convection fills the cell, or to a state in which the entire cell is quiescent, depending on the direction of its propagation. In making figure 16, we set the Rayleigh number very close to the value at which the front velocity is zero. As a consequence, this 'transient' actually lasted for many days, allowing us to make an essentially steady-state image of the flow. Slightly more than one full cycle of the travelling-wave oscillation is shown.

In the top image in figure 16, the rightmost roll is outlined in white by clockwise-circulating, ethanol-rich fluid. As time progresses during the first half-cycle of the oscillation, this roll moves to the right, decreasing in vertical extent and disappearing into the top surface of the cell. In the second half-cycle, a corresponding,

counterclockwise-circulating, ethanol-poor roll decreases in vertical extent and moves down into the lower surface of the cell. Thus, during the first half-cycle, ethanol-rich fluid is pumped laterally into the top half of the fluid layer just outside the front, and ethanol-poor fluid is pumped into the lower half during the second half-cycle. Averaged in time, this process enhances the stabilizing density stratification produced in the quiescent part just beyond the front region by the Soret effect. By this mechanism, convection is prevented from invading the quiescent region, and the front is stabilized.

These observations conform exactly to the description of a large-scale concentration current given by Linz *et al.* (1988) and Barten *et al.* (1989, 1990, 1991). These authors observed in computations that the phase lag between the concentration and temperature waves in travelling-wave convection causes a time-averaged flux of concentration to be advected in the direction of the roll propagation in the top half of the cell, and a balancing flux in the opposite direction is produced in the bottom half of the cell. Averaged in time, these oppositely propagating fluxes create a pair of half-height, counter-circulating secondary concentration loops at a leading-edge front – see figures 3(b) and 4(c) of Barten *et al.* (1991). These secondary concentration loops are just the time average of the behaviour of the right-most rolls in figure 16. This mechanism of front stabilization appears to be responsible for the stability of a variety of confined states of travelling-wave convection (Barten *et al.* 1991; Kolodner 1991; Surko *et al.* 1991).

Figure 16 is also interesting from the standpoint of the spatiotemporal symmetries exhibited by travelling-wave convection. As discussed above, spatially extended travelling-wave states are antisymmetric with respect to the combined operations of a lateral shift by half a wavelength and a reflection through the horizontal midplane. In a spatially confined state, this symmetry is clearly broken. However, as pointed out by Barten *et al.* (1991), confined states should exhibit an analogous symmetry under a reflection through the midplane combined with a *temporal* shift by half an oscillation period. This symmetry is evident in figure 16, especially including the behaviour of the half-height rolls near the front separating the convecting and non-convecting regions.

Our final transient experiment, shown in figure 17, constitutes the most direct qualitative proof of the existence of the concentration wave which was the original subject of this paper. This experiment also reveals evidence of the backflow fluid component described in the discussion of figures 14(b) and 15. This run began with a well-established state of slow, left-going rolls. Then, at time $t = 0$ in the figure, the Rayleigh number was abruptly set to zero. As indicated by the vertical time bars on the right of the figure, the relaxations of the temperature, velocity, and concentration fields require the definition of several different timescales. By time $t = 30$ s, however, the velocity and temperature fields have decayed essentially to zero, leaving only the slowly diffusing concentration field imprinted in the fluid. As sketched in figure 15, this field consists of alternating regions of high and low ethanol concentration (formerly convective rolls) separated by a continuous region of intermediate concentration (formerly the backflow in figure 15). Because of their differences in buoyancy, the ethanol-rich regions tend to float upwards, and the ethanol-poor regions drift downwards, causing all the former rolls to deform (time $t = 30$ to 70 s in figure 17). If it were not for the neutrally buoyant backflow component, the fluid layer would evolve into a laterally uniform state of high ethanol concentration on top and low concentration on the bottom. However, even after the buoyancy-driven motions have ceased (after time $t = 90$ s in figure 17), the backflow component which

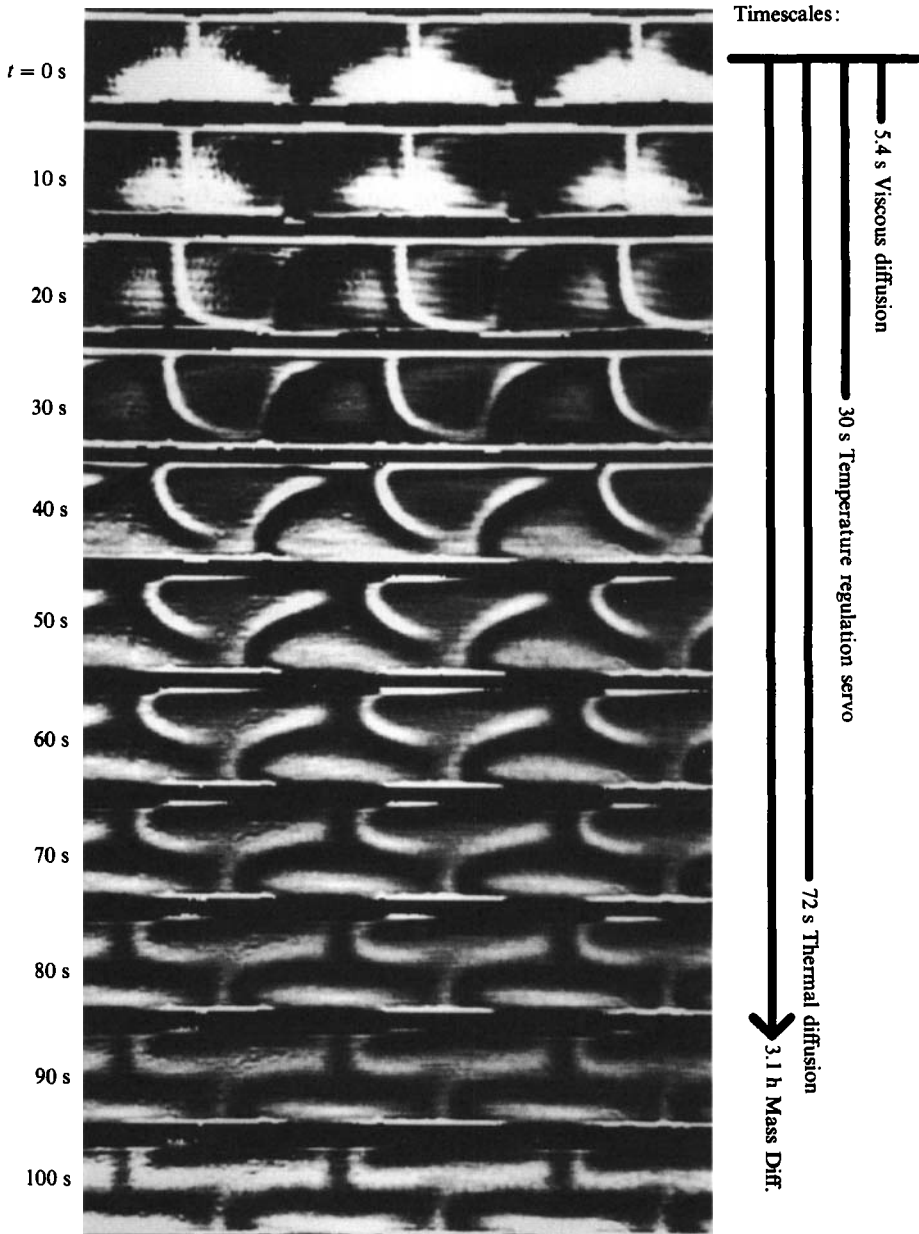


FIGURE 17. Images made every 10 s during an experiment in which a well-developed state of left-going rolls at $r = 1.390$ and $\psi = -0.45$ was quenched by abruptly setting $r = 0$. The time bars on the right of the figure show the vertical viscous, thermal, and mass diffusion times, as well as the timescale for the balancing of the temperature regulation system. After 30 s, the velocity field has completely decayed, the top and bottom plates of the cell are at the same temperature, and the temperature field in the interior of the fluid has decayed by a factor of ~ 60 . Further evolution of the image is therefore due only to differential buoyancy caused by spatial variations in ethanol concentration. The contrast in the bottom image has been enhanced to saturation to show details of the final structure.

marks the boundaries between rolls remains visible, giving the image the appearance of two rows of bricks in a wall.

5. Discussion

In this paper, we have presented visualizations of patterns of travelling-wave convection in ethanol/water mixtures using shadowgraphy from the side. This has turned out to be an extremely powerful technique for studying two-dimensional flows. Because of the strong dependence of the index of refraction on the ethanol concentration, we have been able to make precise quantitative and qualitative observations of the structure of the convective concentration field. We have seen that, in steady states of travelling-wave convection, there is a concentration wave which leads the temperature wave by a sizable phase angle. The amplitude and phase of this concentration wave are associated with the propagation of the pattern. As the Rayleigh number is increased and the propagation slows down, the magnitude of the concentration field is reduced by mixing, and the phase angle approaches $\frac{1}{2}\pi$. The full two-dimensional structure of a travelling-wave state consists of rolls of alternating high and low concentration which are separated by a thin, continuous layer of intermediate concentration. Our separation of the temperature and concentration waves has been based on a small number of *ad hoc* assumptions which, however, appear physically reasonable. This analysis does seem to exhibit some systematic errors, principally seen in the shapes of the profiles of the fundamental concentration component $C_1(z)$ in figure 10(a). There is also a small discrepancy at intermediate phase velocity between the measured phase angle $\phi_C - \phi_T$ and that exhibited by the numerical computations of Barten *et al.* (1989, 1990). Nonetheless, our basic conclusion is that these computations describe the travelling-wave concentration field in minute and quantitative detail. This is an important theoretical achievement which has already borne the fruit of explaining more complex confined travelling-wave states (Barten *et al.* 1991).

Observations of transients have also revealed interesting physical phenomena. The early evolution of linear travelling waves into rolls which rock back and forth with increasing amplitude, entraining fluid from the growing boundary layer into the bulk, or into fully developed, 'overturning' rolls, can be clearly seen in figures 12 and 13. This is because strong optical contrast is caused by exactly the feature of the flow which is associated with these evolutions – the sharp gradients in the concentration field. These qualitative features of developing travelling-wave states have long been heuristically understood, but ours is their first direct observation. A duplication of this sequence of events appears to be within present theoretical capabilities, and such a calculation would be most welcome.

Visualizations of transient flows have also confirmed important notions of large-scale currents which are inherent in travelling-wave patterns. The first of these, a concentration flux which propagates parallel to the phase velocity of the pattern in the upper half of the fluid layer and in the opposite direction in the lower half, appears to be the explanation for the existence of confined states of travelling waves (Barten *et al.* 1991). The observation of this secondary flow in figure 16 is its only direct experimental confirmation. The second large-scale current, the backflow necessitated by the trapping of some of the fluid in the propagating convective rolls, has now been demonstrated in two complementary experiments. It would be most interesting to repeat the photochromic experiments of Moses & Steinberg (1988, 1989) while viewing from the side. In this way, the disadvantages of seeing this flow

only indirectly, as we do, and of integrating out its important vertical structure, as they do, would both be overcome.

We are pleased to acknowledge many useful discussions with B. I. Shraiman, H. R. Brand, C. M. Surko, and M. Lücke. We are particularly indebted to W. Barten for providing us with the results of unpublished numerical computations.

REFERENCES

- BARTEN, W., LÜCKE, M., HORT, W. & KAMPS, M. 1989 Fully developed traveling-wave convection in binary fluid mixtures. *Phys. Rev. Lett.* **63**, 376–379.
- BARTEN, W., LÜCKE, M. & KAMPS, M. 1990 Structure and dynamics of nonlinear convective states in binary fluid mixtures. In *Proc. NATO Advanced Research Workshop on Nonlinear Evolution of Spatio-temporal Structures in Dissipative Continuous Systems* (ed. F. H. Busse & L. Kramer), pp. 131–148. Plenum.
- BARTEN, W., LÜCKE, M. & KAMPS, M. 1991 Localized traveling-wave convection in binary-fluid mixtures. *Phys. Rev. Lett.* **66**, 2621–2625.
- BENSIMON, D., KOLODNER, P., SURKO, C. M., WILLIAMS, H. L. & CROQUETTE, V. 1990 Competing and coexisting dynamical states of traveling-wave convection in an annulus. *J. Fluid Mech.* **217**, 441–467.
- BENSIMON, D., PUMIR, A. & SHRAIMAN, B. I. 1989 Nonlinear theory of traveling wave convection in binary mixtures. *J. Phys. Paris* **50**, 3089–3108.
- EATON, K. D., OHLSEN, D. R., YAMAMOTO, S. Y., SURKO, C. M., BARTEN, W., LÜCKE, M., KAMPS, M. & KOLODNER, P. 1991 Concentration field in traveling-wave and stationary convection in fluid mixtures. *Phys. Rev. A* **43**, 7105–7108.
- HURLE, D. T. J. & JAKEMAN, E. 1971 Soret-driven thermosolutal convection. *J. Fluid Mech.* **47**, 667–689.
- KOLODNER, P. 1990 Neutrally stable fronts of slow convective traveling waves. *Phys. Rev. A* **42**, 2475–2478.
- KOLODNER, P. 1991 Drift, shape, and intrinsic destabilization of pulses of traveling-wave convection. *Phys. Rev. A* **43**, 6448–6465.
- KOLODNER, P., PASSNER, A., SURKO, C. M. & WALDEN, R. W. 1986 Onset of oscillatory convection in a binary fluid mixture. *Phys. Rev. Lett.* **56**, 2621–2624.
- KOLODNER, P., PASSNER, A., WILLIAMS, H. L. & SURKO, C. M. 1987 The transition to finite-amplitude traveling-wave convection in binary fluid mixtures. *Nucl. Phys. B (Proc. Suppl.)* **2**, 97–108.
- KOLODNER, P. & WILLIAMS, H. L. 1990 Complex demodulation techniques for experiments on traveling-wave convection. In *Proc. NATO Advanced Research Workshop on Nonlinear Evolution of Spatio-temporal Structures in Dissipative Continuous Systems* (ed. F. H. Busse & L. Kramer), pp. 73–92. Plenum.
- KOLODNER, P., WILLIAMS, H. & MOE, C. 1988 Optical measurement of the Soret coefficient of ethanol/water solutions. *J. Chem. Phys.* **88**, 6512–6524.
- LINZ, S. J. & LÜCKE, M. 1987 Convection in binary mixtures: a Galerkin model with impermeable boundary conditions. *Phys. Rev. A* **35**, 3997–4000.
- LINZ, S. J., LÜCKE, M., MÜLLER, H. W. & NIEDERLÄNDER, J. 1988 Convection in binary fluid mixtures: traveling waves and lateral currents. *Phys. Rev. A* **38**, 5727–5741.
- MOSES, E., FINEBERG, J. & STEINBERG, V. 1987 Multistability and confined traveling-wave patterns in a convecting binary mixture. *Phys. Rev. A* **35**, 2757–2760.
- MOSES, E. & STEINBERG, V. 1988 Mass transport in propagating patterns of convection. *Phys. Rev. Lett.* **60**, 2030–2033.
- MOSES, E. & STEINBERG, V. 1989 Mass transport in propagating patterns of convection. *Physica* **37D**, 341–358.
- OHLSEN, D. R., YAMAMOTO, S. Y., SURKO, C. M. & KOLODNER, P. 1990 Transition from traveling-wave to stationary convection in fluid mixtures. *Phys. Rev. Lett.* **65**, 1431–1434.

- RASENAT, S., HARTUNG, G., WINKLER, B. L. & REHBERG, I. 1989 The shadowgraph method in convection experiments. *Exp. Fluids* **7**, 412–419.
- STEINBERG, V. & KAPLAN, E. 1991 Localized and ‘blinking’ traveling wave patterns in a convective binary mixture. In *Proc. NATO Advanced Research Workshop on Spontaneous Formation of Space–Time Structures and Criticality* (ed. T. Riste & D. Sherrington), pp. 207–244. Plenum.
- STEINBERG, V., MOSES, E. & FINEBERG, J. 1987 Spatio-temporal complexity at the onset of convection in a binary fluid. *Nucl. Phys. B (Proc. Suppl.)* **2**, 109–124.
- SURKO, C. M. & KOLODNER, P. 1987 Oscillatory traveling-wave convection in a finite container. *Phys. Rev. Lett.* **58**, 2055–2058.
- SURKO, C. M., OHLSEN, D. R., YAMAMOTO, S. Y. & KOLODNER, P. 1991 Confined states of traveling-wave convection. *Phys. Rev. A* **43**, 7101–7104.
- WALDEN, R. W., KOLODNER, P., PASSNER, A. & SURKO, C. M. 1985 Traveling waves and chaos in convection in binary fluid mixtures. *Phys. Rev. Lett.* **55**, 496–499.